An InSAR-Based Method for Predicting Long-Term Land Subsidence in Goafs through the Concatenation of Multiple Short-Term Monitoring Data

Jinyang Li , Mingdong Zang * , Nengxiong Xu , Gang Mei , Sen Yang

Posted Date: 18 July 2023

doi: 10.20944/preprints202307.1115.v1

Keywords: InSAR-based method; coal mine goaf; prediction of long-term land subsidence; concatenation of multiple short-term monitoring data

Article

An InSAR-Based Method for Predicting Long-Term Land Subsidence in Goafs through the Concatenation of Multiple Short-Term Monitoring Data

Jinyang Li [1,2], Mingdong Zang [1,2,3,4,*], Nengxiong Xu [1,3,4], Gang Mei [1,3,4] and Sen Yang [1]

[1] School of Engineering and Technology, China University of Geosciences (Beijing), Beijing, 100083, China; Jinyang.Li@email.cugb.edu.cn (J.L.); xunengxiong@cugb.edu.cn (N.X.); gang.mei@cugb.edu.cn (G.M.); SenYang@email.cugb.edu.cn (S.Y.)

[2] Observation and Research Station of Ground Fissure and Land Subsidence, Ministry of Natural Resources, Xi'an, Shaanxi, 710054, China

[3] Institute of Geosafety, China University of Geosciences (Beijing), Beijing, 100083, China

[4] Engineering and Technology Innovation Center for Risk Prevention and Control of Major Project Geosafety, Ministry of Natural Resources of the People's Republic of China, Beijing, 100083, China

* Correspondence: mzang@cugb.edu.cn; Tel.: +86-10-82322627

Abstract: The land subsidence occurring in goafs after coal mining is a protracted process. The accurate prediction of long-term land subsidence in goafs relies heavily on the availability of long-term monitoring data. However, the scarcity of continuous long-term land subsidence monitoring data subsequent to the cessation of mining significantly hinders the accurate prediction of long-term land subsidence in goafs. To address this challenge, this study proposes an innovative method based on Interferometric Synthetic Aperture Radar (InSAR) for predicting long-term land subsidence of goafs following coal mining. The proposed method employs a concatenation approach that integrates multiple short-term monitoring data from different coal faces, each with distinct cessation times, into a cohesive and uniform long-term sequence by normalizing the subsidence rates. The method was verified using actual monitoring data from the Yangquan No.2 mine in Shanxi Province, China. Initially, coal faces with same shapes but varying cessation times were selected for analysis. Using InSAR monitoring data collected between June and December of 2016, the average subsidence rate corresponding to the duration after coal mining cessation of each coal face was back-calculated. Subsequently, a function relating subsidence rate to the duration after coal mining cessation was fitted to the data. Finally, the relationship between cumulative subsidence and the duration after coal mining cessation was derived by integrating the function. The results indicated that the relationship between subsidence rate and duration after coal mining cessation followed an exponential function for a given coal face, whereas the relationship between cumulative subsidence and duration after coal mining cessation conformed to the Knothe time function. Notably, after the cessation of coal mining, significant land subsidence persisted in the goaf of the Yangquan No.2 mine for a duration ranging from 5 to 10 years. The cumulative subsidence curve along the long axis of the coal face ultimately exhibited an inclined W-shape. The proposed method enables the quantitative prediction of residual land subsidence in goafs, even in cases where continuous long-term monitoring data are insufficient, thus providing valuable guidance for construction decisions above the goaf.

Keywords: InSAR-based method; coal mine goaf; prediction of long-term land subsidence; concatenation of multiple short-term monitoring data

1. Introduction

Coal resources are the basis for economic development and social progress, but coal mining often creates large underground cavities that then induce significant land subsidence [1–3], which is

 doi:10.20944/preprints202307.1115.v1

a long-term process that poses a great harm to ground structures. The accurate prediction of long-term land subsidence in the goaf is critical to ensuring the stability of the goaf site's engineering construction [4,5].

Methods for predicting residual land subsidence have been proposed since the 1990s [6]. There are two main types of methods to predict residual land subsidence in mining areas. First, a mathematical or mechanical method can derive the formula of residual subsidence factors based on the stress-strain relationship of collapsed rocks, including the limit subsidence prediction method [7,8], the numerical simulation prediction method [9], and the nonlinear prediction method [10,11]. Subsequently, a time function or a creep model can be employed to establish the long-term subsidence prediction model [12–14]. Second, the inversion method can predict long-term subsidence based on the analysis of a period of monitoring data [15–17]. As rock movement and land subsidence in mining areas are complex problems with many factors implicated, mathematical and mechanical methods frequently encounter difficulties in selecting calculation parameters during the residual land subsidence prediction [18,19]. The problem becomes more serious when the time factor is considered, but this complication can be avoided by using inversion methods through the analysis of monitoring data, which allow for a more direct analysis and prediction of long-term land subsidence at a specific site, as well as more reliable results derived from actual monitoring data. Site investigations such as leveling surveys and the Global Position System (GPS) are an earlier method to monitor the land subsidence [20,21]. However, high costs, long observation periods, and complex terrains limit the application of such conventional monitoring methods in large areas and long periods of time [22,23]. In recent years, a new technology, Interferometric Synthetic Aperture Radar (InSAR), has been widely used to predict long-term land subsidence in mining areas, with the advantages of all-weather measurement, short monitoring periods, large monitoring areas, and intuitive and reliable data [24,25]. Gabriel et al. first demonstrated the possibility of using the Differential InSAR (D-InSAR) technique for detecting land subsidence at the centimeter scale [26]. Subsequently, a series of comprehensive experiments was carried out to monitor land subsidence over a goaf with SAR images, laying the groundwork for future research on land subsidence in mining areas using InSAR data [27–29]. The small-baseline subset (SBAS) technique, a kind of InSAR monitoring technique, is considered effective for monitoring land micro-subsidence in large mining areas [30]. This method effectively increases the temporal resolution of monitoring data, solves the destructive problem caused by long baselines between different SAR datasets, and separates the topographic residual phase from atmospheric noise, making the subsidence monitoring results more accurate and reliable [31,32]. Currently, the SBAS-InSAR technology has been widely used to monitor land subsidence. Solaro et al. used this technique to monitor the land subsidence of a Hawaiian volcano. In their study, the SBAS-InSAR technique was first applied to the interference processing of SAR data in different modes[33]. Liu et al. used the same technique to study the land subsidence induced by coal mining in Yangquan, Shanxi Province, China, and assessed its potential damage to ground facilities [34]. Some scholars use the short-term monitoring data obtained by InSAR technology for parameter inversion and then employ other mathematical methods to carry out prediction studies on long-term land subsidence in the goaf. Fan et al. used a probabilistic integral method model in conjunction with InSAR to predict land subsidence in mining areas [35]. Yang et al. established a functional model between all parameters of the probabilistic integral method and InSAR Line-Oriented Simulation (LOS) directional strain, and introduced a Boltzmann function to improve the functional model to realize the prediction of full basin subsidence of the mine area under various mining degrees [36,37].

Despite the growing interest in predicting long-term land subsidence in goafs, challenges persist and must be addressed. First, the abovementioned applications strongly depend on continuous and long-term monitoring data. However, field observations generally end when coal mining stops, and it becomes difficult to obtain continuous and long-term monitoring data of the area, limiting the application of InSAR-based prediction methods for long-term goaf land subsidence [38–40]. Second, when handling long time series of InSAR monitoring data, the iterative calculation process can introduce a significant number of errors, leading to reduced accuracy in predicting long-term land subsidence [41]. The accumulation of these errors can negatively impact the reliability of the

 doi:10.20944/preprints202307.1115.v1

predictions made. Therefore, careful attention must be paid to the error analysis and mitigation strategies used during the iterative calculation process to ensure accurate and robust predictions of long-term land subsidence.

The present work introduces a novel approach for predicting long-term land subsidence in goafs. By normalizing short-term InSAR monitoring data into a time-series subsidence rate curve, this method links land subsidence to the duration after coal mining cessation. This solution addresses the challenges of temporal and spatial discontinuity in InSAR monitoring data for mining-area subsidence, enhancing accuracy by minimizing the errors involved in prolonged monitoring. Consequently, it provides accurate predictions of long-term land subsidence even in cases where monitoring duration is limited.

This paper describes the site characteristics of the study area in detail, presents a thorough explanation of the data processing and prediction process, and finally discusses the results of land subsidence assessment, as well as the applicable conditions of the proposed method.

2. Methodology

A goaf typically comprises multiple coal faces. As the mining depth, coal thickness, overburden configuration, and surface topography of each coal face differ, it is not feasible to arbitrarily correlate the land subsidence monitoring data of various coal faces. The method proposed in this paper addresses these issues by utilizing short-term land monitoring data obtained through the SBAS-InSAR technology. The land subsidence data obtained from remote sensing images cover the entire mining area. Additionally, by obtaining data for the entire mining area in a single monitoring event, the potential for errors and inconsistencies that could occur if separate monitoring efforts were conducted for each individual coal face is eliminated. Simultaneously, by choosing multiple coal faces within a close proximity in the mining area as the subject of analysis, it can significantly ensure that the mining depth, coal seam thickness, overburden configuration, and surface form are consistent or comparable, thereby avoiding the issue where multiple data cannot be correlated due to the confounding effects of various complex conditions. Figure 1 outlines the procedure for predicting land residual subsidence in goafs. The proposed approach consists of the following phases:

Preprints (www.preprints.org) | NOT PEER-REVIEWED | Posted: 18 July 2023 doi:10.20944/preprints202307.1115.v1

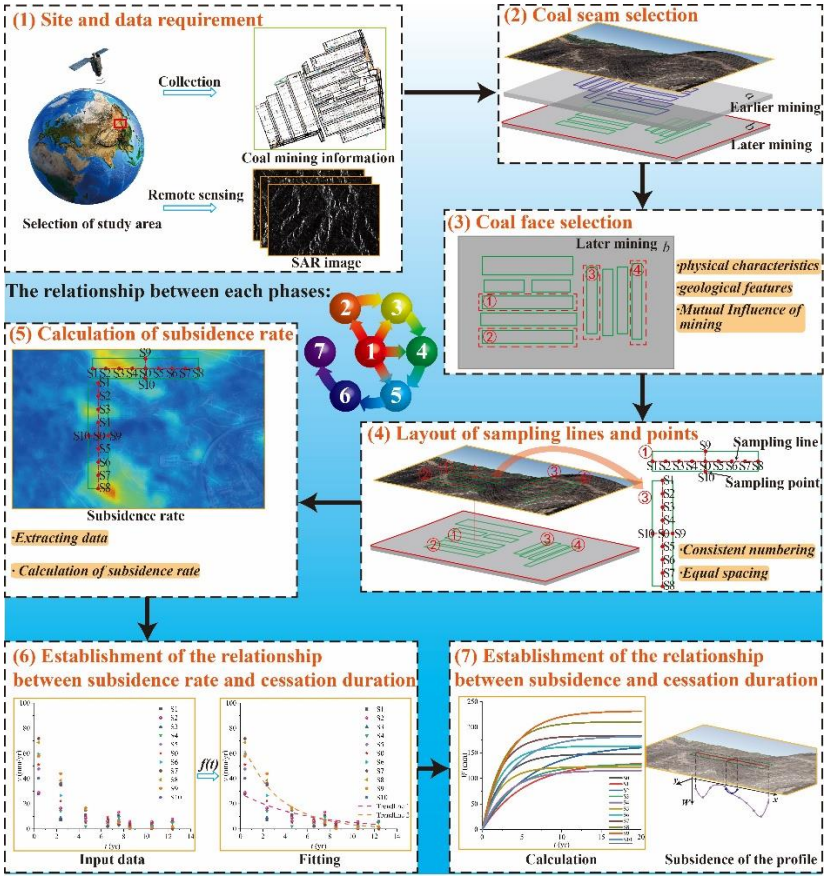

Figure 1. Flowchart showing steps involved in predicting long-term land subsidence in a goaf.

(1) Site and data requirement. A goaf with a single geological condition was selected as the study area. Information regarding the coal seam mining, a coal face arrangement diagram, and a survey report of the study area are needed. To ensure the reliability of the monitoring data when applying the method proposed in this research, it is crucial to maintain their consistency. By employing the same monitoring method, conditions, and accuracy for the goaf formed by each coal face, we can guarantee the uniformity of the monitoring data for the goafs formed by different coal faces. When using traditional on-site monitoring methods to track the land of the goaf above each coal face, the subsidence data obtained can be relatively independent. As a result, errors between monitoring data from different positions are inevitable. However, SBAS-InSAR monitoring data offers a solution to this issue. With its wide coverage and continuous observation, a single measurement can cover the entire mine area, including the surface area above all coal faces. This ability ensures consistency in the monitoring data, meeting the abovementioned data requirement.

(2) Coal seam selection. Based on the available information, the coal seam mining situation in the study area was assessed, and the coal seams that had the most significant impact on the goaf were identified. Specifically, the most recently mined coal seam was selected as the main focus of the research. The study aimed to investigate the arrangement of coal faces in the studied seam, and to determine whether the goaf in the area could be classified as a repeated mining situation if other coal seams had been excavated above it.

(3) Coal face selection. Previous studies have identified several main factors that influence mining operations [42]. Therefore, when selecting multiple coal faces under the same seam, it is essential to consider the thickness of the coal seam, mining depth, seam inclination, overburden configuration, mining width, and coal mining method for each face. To ensure the methodological reliability of the data transformation process, we selected several coal faces that shared the factors mentioned above. Specifically, if the selected coal faces had similar shapes and sizes, and were in close proximity, it was possible to unify the above factors to a certain extent, which helped to

 doi:10.20944/preprints202307.1115.v1

minimize their influence on the results. Meanwhile, each coal face was numbered based on the order in which coal mining ceased, from the most recently active coal face to the oldest. It is important to note that if other coal faces are being mined or have recently been stopped near the selected coal faces, their land subsidence may overlap with the studied subsidence, which could impact the accuracy of the results. To determine the scope of land subsidence caused by mining coal faces in this mine, an empirical formula can be used [43]. It is crucial to choose a coal face that is not near other active or recently stopped mining operations to ensure accurate monitoring results. It is also essential to ensure that the thickness and number of coal seams mined in the study area are consistent. The selected series of coal faces should be in the same coal seam, and the upper mined coal seam should be in a similar condition (e.g., similar physical characteristics and geological features), as this will help to ensure that the study results are reliable and can be compared accurately.

(4) Layout of sampling lines and points. The sampling line passed through the center of the selected coal face and was perpendicular to the boundary, with equivalent spacing between adjacent sampling points. Meanwhile, the sampling points were numbered sequentially, and those in the same location on each coal face were numbered consistently.

(5) Calculation of subsidence rate. The data from the selected sampling points were extracted from the short-term InSAR monitoring data of the study area and then used to calculate the average subsidence rate at each sampling point.

(6) Establishment of the relationship between subsidence rate and duration after coal mining cessation. The duration after coal mining cessation for each coal face was calculated based on the previous step, and a rectangular plane coordinate system was established for each point using duration after coal mining cessation as the horizontal coordinate and average subsidence rate as the vertical coordinate. The data from the sampling points with same identification number in each coal face were then input into the corresponding coordinate system. To obtain the curve representing the relationship between subsidence rate and duration after coal mining cessation, the data points in each coordinate system were fitted to a time function.

(7) Establishment of the relationship between subsidence and duration after coal mining cessation. The subsidence rate was then integrated over time to determine the relationship between subsidence and duration after coal mining cessation. By combining this information with the position of each sampling point, the cumulative subsidence change of the profile along sampling line was obtained.

3. Application

In this section, we evaluate the method using an example from the mining area of Yangquan No.2 mine, which is situated in the Qinshui coalfield, the largest coal-producing Carboniferous Triassic coalfield in China. We performed the following steps to complete the evaluation process, with each step discussed in detail below.

3.1. Study area

The study area is located at the northeastern part of the Qinshui coalfield, approximately 5 km southwest of Yangquan, eastern Shanxi Province (Figure 2). The study area is characterized by deeply incised valleys and high mountains, with an elevation ranging from 700 m to 1246.9 m above sea-level (Figure 2) and a maximum relative elevation difference of more than 540 m. The surface is exposed bedrock with little vegetation in most areas. Two rivers, the Taohe river and the Xiaohe river, pass through the Yangquan area, which are distributed as dendritic drainages (Figure 3).

Preprints (www.preprints.org) | NOT PEER-REVIEWED | Posted: 18 July 2023 doi:10.20944/preprints202307.1115.v1

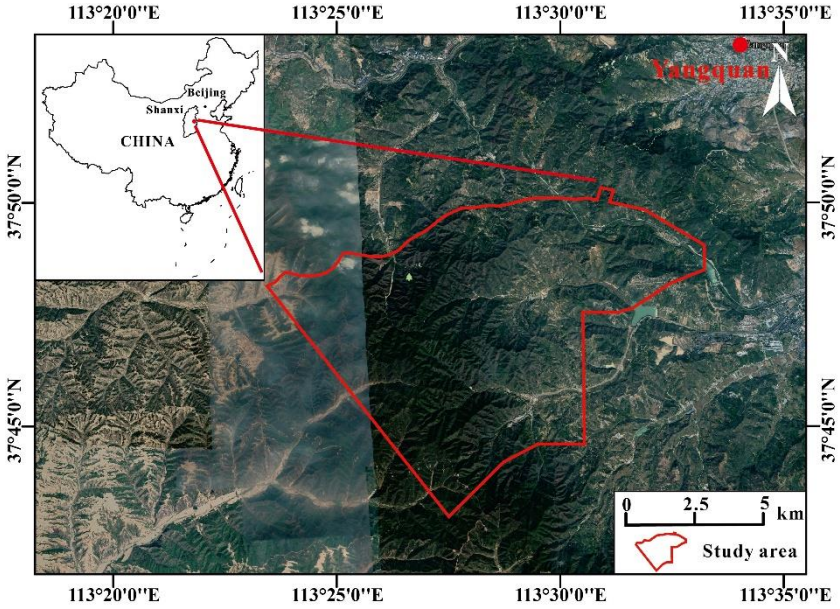

Figure 2. Location of the study area.

The exposed strata in the study area have an age that varies from the Lower Triassic (T_1) to the Lower Permian (P_1). These strata include sandy mudstone interspersed with feldspathic sandstone of the Heshanggou Formation, felsic sandstone intercalated with sandy mudstone of the Liujiagou Formation, and sandstones, shales, muddy sandstones, sandy mudstones, and mudstones of the Upper Shihezi and Lower Shihezi formations, as shown in Figure 3.

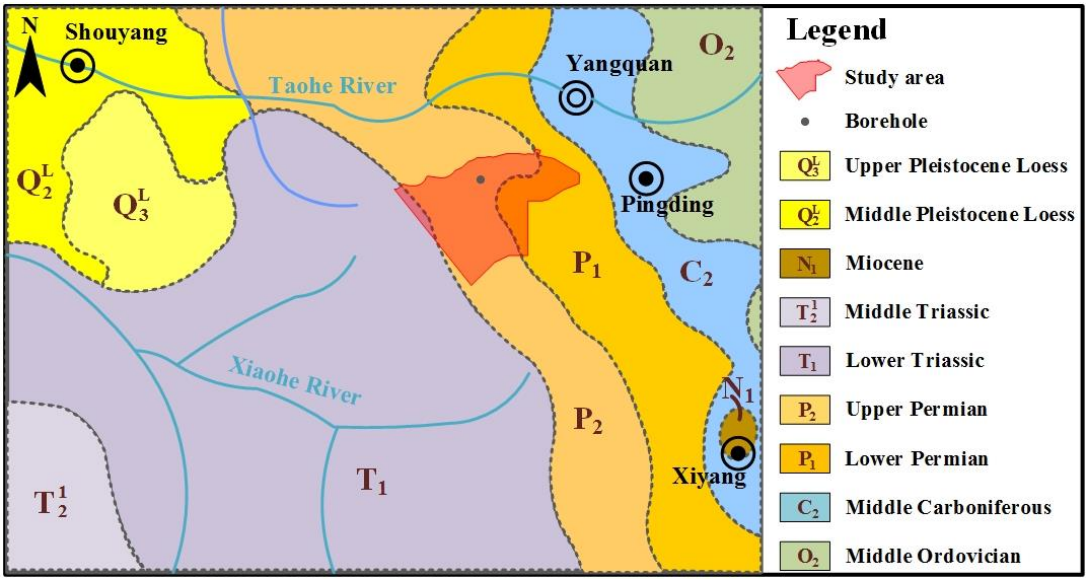

Figure 3. Geological map of the study area.

We drilled a borehole to investigate the stratigraphic profile from the mining area surface to a depth of 413.95 m. The observed strata encompass various geological ages, ranging from the Upper Permian to the Upper Carboniferous periods. Specifically, from the surface down to 246.38 m, the strata comprise the Shiqianfeng Formation, the Upper Shihezi Formation, and the Lower Shihezi Formation. At depths between 307.48 m and 413.95 m, the strata transition into the Shanxi Formation and the Taiyuan Formation with increasing depth, as seen in Figure 4.

Preprints (www.preprints.org) | NOT PEER-REVIEWED | Posted: 18 July 2023 doi:10.20944/preprints202307.1115.v1

Formation	Total Depth /m	Strayum Thickness /m	Column chart	Rock name	Lithological description
Shanxi Fm	246.38	246.38			Drilling without coring.
	247.88	1.50		Sandy mudstone	Dark gray, brittle lithology, containing a small amount of mica fragments and more gravel.
	260.25	12.37		Medium sandstone	Dark gray, brittle lithology, containing a small amount of mica fragments and more gravel.
	262.26	2.01		3#Coal	Hard and lustrous.
	262.65	0.39		Mudstone	Drey-black and dense, containing a small amount of carbonaceous, aluminous material and plant fossils.
	307.48	44.83			Drilling without coring.
Taiyuan Fm	317.22	9.74		Mudstone and Sandstone	Interbedded structure of dark gray fine-grained sandstone and sandy mudstone, fine-grained sandstone in the upper part and sandy mudstone in the lower part.
	319.47	2.25		Sandy mudstone	Black, containing more sand grains above and less below, with pyrite and a little carbonaceous at the bottom.
	322.74	3.27		8#Coal	Hard and lustrous, with the structure of 1.98 (0.05) 1.01 (0.07) 0.16.
	326.93	4.19		Mudstone	Black and dense, brittle lithology, containing little charcoal, plant fossils and localized sand grains.
	330.56	3.33		9#Coal	Hard and lustrous, with the structure of 0.63 (0.20) 2.50.
	334.96	13.85			Drilling without coring.
	348.74	3.78		Mudstone	Dark gray, containing sand grains with black lines.
	349.63	0.89		12#Coal	Hard and shiny, with the structure of 0.58 (0.26) 0.05.
	351.03	1.40		Mudstone	Black /dark gray, soft lithology, fossiliferous mudstone containing aluminium.
	352.53	1.50		Sandy mudstone	Dark gray, sandy mudstone containing sand grains with black lines in the surface.
	354.13	1.60		Fine sandstone	Grey, clayey cemented, fine-grained sandstone with black lines, containing charred plant fossils.
	358.18	4.05		Mudstone	Black and dense, brittle lithology, containing stellate pyrite and calcareous mudstone at the bottom.
	361.24	3.06		Limestone	Dark gray, soft mud-bearing lithology, containing plant fossils and calcareous mudstone at the bottom.
	362.04	0.80		13#Coal	Lustrous.
	383.32	21.23			Drilling without coring.
	383.62	0.30		14#Coal	Hard and lustrous.
	387.87	4.25		Mudstone	Black, brittle lithology, containing pyrite and small iron grains.
	393.80	5.93		15#Coal	Hard and lustrous, with the structure of 2.07 (0.10) 2.00 (0.10) 1.66.
	397.63	3.83		Mudstone	Black, containing a lot of plant fossils, a few aluminous and mica fragments, with coal debris and small grains in the lower part.
	402.75	5.12		Sandy mudstone	Black gray, nodular sandy mudstone with black lines, containing plant fossils in the upper part.
	413.95	11.20		Gritstone	Coarse-grained sandstone with conglomerate and mudstone fragments, dominated by quartz and feldspar, containing mica and black minerals.

Figure 4. Borehole diagram. The location of the borehole is shown in Figure 3.

3.2 Selection of coal faces and layout of sampling lines and points

The Yangquan No.2 mine has three coal seams, 3#, 8#, and 15#, with average thicknesses of 1.96 m, 2.26 m, and 6.42 m, respectively. The comprehensive mechanized roof release coal mining method is used for these coal seams, which involves a backward coal mining method toward the long wall, and the fully caving method is used for roof management. Currently, the 3#, 8#, and 15# coal seams have been mined in the study area, with the 8# coal seam only distributed in a small area in the southwestern part of the study area. Most of the study area is a two-layer mining area. The 15# coal seam was mined later than the upper 3# coal seam, which meets the requirement of the re-mining condition. Therefore, we selected coal faces based on the area of the 15# coal seam. The selected coal faces are rectangles concentrated in the northeast of the study area. The long axis of the rectangle is parallel to the mining direction, whereas the short axis is perpendicular to the mining direction. The location and subsidence rate of the selected coal faces within the study area are shown in Figure 5a. As all the coal mining operations were stopped after the monitoring data were collected, our analysis

Preprints (www.preprints.org) | NOT PEER-REVIEWED | Posted: 18 July 2023 doi:10.20944/preprints202307.1115.v1

and research are facilitated. Table 1 shows the time interval between monitoring and the cessation of coal mining for the selected coal face.

To study long-term land subsidence in the study area, we used the SBAS-InSAR technique to process eight-view RADARSAT-2 images from June to December of 2016 [34], resulting in a raster map of land subsidence rates. InSAR data were collected from multiple monitoring points above the selected coal face, and we arranged sampling lines to study the subsidence characteristics of representative locations. Two sampling lines were set in each roughly rectangular coal face, one parallel to the long axis and one parallel to the short axis, with sampling points arranged along the lines (Figure 5b).

For each coal face, we first set the intersection of the two sampling lines as point 0 (S0). We placed 10 additional sampling points along the mining direction, numbered from 1 to 10 (S1–S10), with S1 and S10 on the boundary of the long axis (Figure 5b). We also placed eight additional points perpendicular to the mining direction, numbered from 11 to 18 (S11–S18), with S11 and S18 on the boundary of the short axis (Figure 5b). This arrangement was used consistently across all coal faces, with the sampling points equally spaced and numbered for consistency. The sampling points at the same relative locations in the different coal faces were numbered consistently and can be considered to have same conditions. This arrangement allows for the precise and consistent sampling of the coal face to ensure accurate measurements.

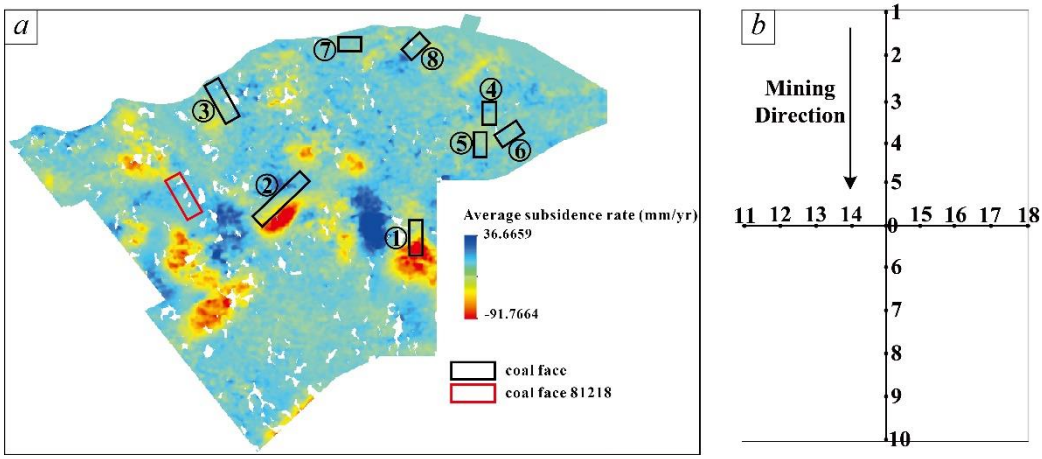

Figure 5. Map showing the average subsidence rate of the study area and the location of selected coal faces: (a) average subsidence rate of the study area based on InSAR data from June to December of 2016; (b) schematic diagram of the sampling lines and points in each coal face.

Table 1. Information on the selected coal faces.

Number	The cessation year of coal mining	Time interval between monitoring and cessation of coal mining (yr)
1	2016	0.5
2	2014	3
3	2012	5
4	2010	7
5	2009	8
6	2008	9
7	2006	11
8	2004	13

3.3 Relationship between subsidence rate and duration after coal mining cessation

We extracted the monitoring data at each sampling point and identified the corresponding duration after coal mining cessation based on Table 1. Using these data, we obtained the average

Preprints (www.preprints.org) | NOT PEER-REVIEWED | Posted: 18 July 2023 doi:10.20944/preprints202307.1115.v1

subsidence rate for each sampling point from eight different coal faces (Table 1). As the duration after coal mining cessation corresponds to the number of coal faces, we then established a rate-time coordinate system to show the relationship between subsidence rate and duration after coal mining cessation. For each time interval between monitoring and cessation of coal mining, the subsidence rate of each point is plotted as a dot (Figure 6).

As the sampling points in the same relative locations on each coal face were consistently numbered, those with the same label numbers were grouped for further research such that all sampling points with number S0 were grouped into the first group, those with number S1 were grouped into the second group, and so on. The sampling points were grouped into 19 groups, from S0 to S18. In each group, the sampling points came from eight different coal faces, with eight different durations after coal mining cessation from 0.5 yr to 13 yr (Table 1). An exponential function was used to fit the data from each group, as seen in Figure 6. The functional form is as follows:

$$v(t) = v_0 e^{-ct}, \tag{1}$$

where $v(t)$ is the average subsidence rate, which depends on the duration after coal mining cessation, v_0 is the initial subsidence rate after the cessation of coal mining, c is the amplitude curve variation, and t is the duration after coal mining cessation.

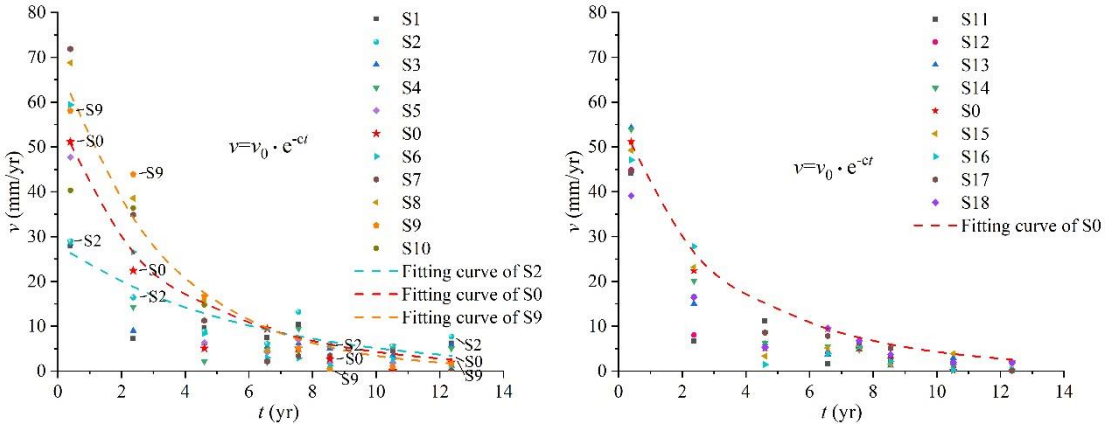

Figure 6. Subsidence rate versus duration after coal mining cessation for each sampling point: (a) along the long axis of the coal face; (b) along the short axis of the coal face.

Figure 6 shows that the sampling points in each group can be fitted with Eq. (1). The regression parameters of each group are listed in Table 2. For each group, the overall subsidence rate exhibits a rapid initial decrease followed by a slower one. The subsidence rate declines notably during the first 5 years after the cessation of coal mining, whereas the decreasing trend appears to level off after 5 years (Figure 6). Along the long axis of the coal face, the subsidence rate curve shows two distinct patterns (Figure 6a). Taking S2, near the upper boundary (Figure 5b), as an example. The overall subsidence rate of S2 shows a slow decreasing trend. The subsidence rate gradually declines at a roughly uniform pace during the first 5 years following the cessation of coal mining. It remains stable for the next 5 years before experiencing a slight increase after 13 years (Figure 6a). The maximum subsidence rate occurred at half a year after the cessation of coal mining with a value of 28.9 mm/yr, whereas the minimum subsidence rate occurred at the 10th year after the cessation of coal mining with a value of 5.5 mm/yr (Figure 6a). The variation trend of subsidence rate at S1, S3, and S4 is similar to that at S2. Taking S9 near the lower boundary (Figure 5b) as another example, its subsidence rate sharply decreases during the first 5 years after the cessation of coal mining, following a slower decline during the 5–13 years after the cessation of coal mining (Figure 6a). The maximum subsidence rate occurred at half a year after the cessation of coal mining with a value of 58.1 mm/yr, whereas the minimum subsidence rate occurred at the 9th year after the cessation of coal mining with a value of 0.28 mm/yr (Figure 6a). The variation trend of subsidence rate at S7, S8, and S10 was similar to that

Preprints (www.preprints.org) | NOT PEER-REVIEWED | Posted: 18 July 2023 doi:10.20944/preprints202307.1115.v1

at S9. The subsidence rate of S0 gradually decreases after the cessation of coal mining until the 13th year, and the points next to it have similar variation trends. Along the short axis of the coal face, the subsidence rate patterns at these sampling points were similar, with fitting curves indicating a consistent subsidence rate over time (Figure 6b). Each sampling point on this line shows a subsidence rate similar to the central point (S0), with little variation over time (Figure 6b).

Table 2. Regression parameters of the function modeling subsidence rate and cumulative subsidence over time.

Point	*v*-*t* function	*W*-*t* function	v_0	c	W_m	R^2 (%)
0	$v = 59.474e^{-0.403t}$	$W = 147.612(1-e^{-0.403t})$	59.474	0.403	147.612	96.9
1	$v = 24.784e^{-0.188t}$	$W = 131.809(1-e^{-0.188t})$	24.784	0.188	131.809	65.9
2	$v = 28.131e^{-0.170t}$	$W = 165.507(1-e^{-0.170t})$	28.131	0.170	165.507	80.6
3	$v = 32.830e^{-0.258t}$	$W = 127.261(1-e^{-0.258t})$	32.830	0.258	127.261	81.5
4	$v = 36.495e^{-0.316t}$	$W = 115.539(1-e^{-0.316t})$	36.495	0.316	115.539	80.6
5	$v = 56.310e^{-0.460t}$	$W = 122.309(1-e^{-0.460t})$	56.310	0.460	122.309	97.7
6	$v = 70.860e^{-0.435t}$	$W = 162.994(1-e^{-0.435t})$	70.860	0.435	162.994	99.7
7	$v = 81.562e^{-0.446t}$	$W = 182.919(1-e^{-0.446t})$	81.562	0.446	182.919	98.9
8	$v = 80.975e^{-0.385t}$	$W = 210.373(1-e^{-0.385t})$	80.975	0.385	210.373	99.1
9	$v = 69.678e^{-0.301t}$	$W = 231.842(1-e^{-0.301t})$	69.678	0.301	231.842	95.5
10	$v = 49.958e^{-0.274t}$	$W = 182.281(1-e^{-0.274t})$	49.958	0.274	182.281	90.9
11	$v = 56.152e^{-0.544t}$	$W = 103.222(1-e^{-0.544t})$	56.152	0.544	103.222	90.9
12	$v = 57.035e^{-0.548t}$	$W = 103.994(1-e^{-0.548t})$	57.035	0.548	103.994	94.0
13	$v=67.484e^{-0.574t}$	$W = 117.528(1-e^{-0.574t})$	67.484	0.574	117.528	98.4
14	$v = 64.033e^{-0.460t}$	$W = 139.256(1-e^{-0.460t})$	64.033	0.460	139.256	98.9
15	$v=58.353e^{-0.421t}$	$W = 138.536(1-e^{-0.421t})$	58.353	0.421	138.536	97.4
16	$v = 56.574e^{-0.461t}$	$W = 122.639(1-e^{-0.461t})$	56.574	0.461	122.639	95.1
17	$v = 49.485e^{-0.408t}$	$W = 121.197(1-e^{-0.408t})$	49.485	0.408	121.197	96.2
18	$v = 42.968e^{-0.387t}$	$W = 110.963(1-e^{-0.387t})$	42.968	0.387	110.963	94.1

3.4 Relationship between subsidence and duration after coal mining cessation

Integrating the relationship between subsidence rate and duration after coal mining cessation, we can obtain the relationship between cumulative residual subsidence amount and duration after coal mining cessation by integrating Eq. (1) (Figure 7). The function's form after integration is shown in Eq. (2). The regression parameters of each group are listed in Table 2. From Figure 7, the surface of the mining area continued to experience significant subsidence after the coal mining ceased. During the long-term subsidence in the mining area, the maximum residual land subsidence recorded was 232 mm at S9 (Figure 7). After the cessation of coal mining, significant subsidence of the mining area's surface persisted for 5 to 10 years (Figure 7). Within 15 years, 90% of the surface had completed its residual subsidence for all sampling points across the mining area (Figure 7). Subsequently, the subsidence movement stabilized, exhibiting a more consistent and stable growth pattern.

$$W(t) = W_m(1 - e^{-ct}), \quad (2)$$

where $W(t)$ is the subsidence, which depends on the duration after coal mining cessation, W_m is the maximum accumulated subsidence after the cessation of coal mining, and $W_m = v_0/c$.

Preprints (www.preprints.org) | NOT PEER-REVIEWED | Posted: 18 July 2023 doi:10.20944/preprints202307.1115.v1

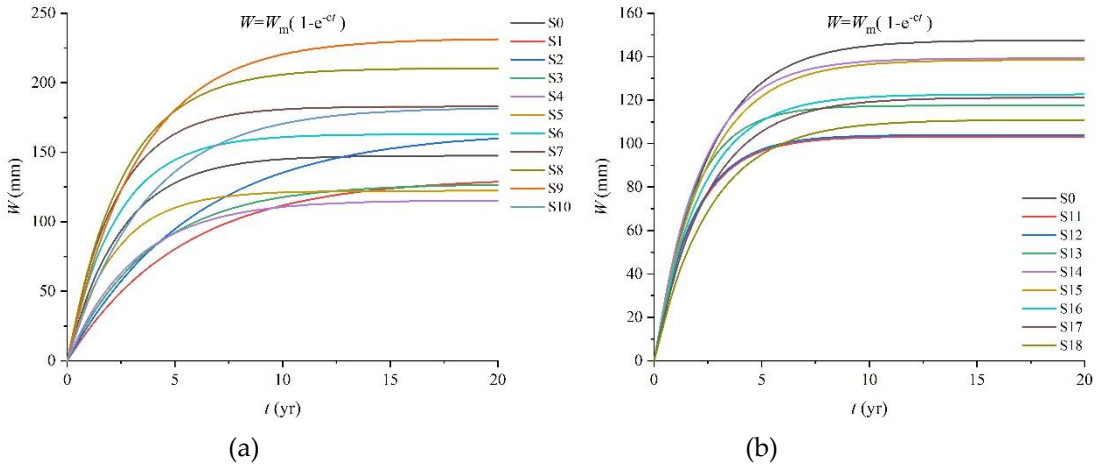

(a) (b)

Figure 7. Subsidence profile obtained by integrating the subsidence rate over time: (a) along the long axis of the coal face; (b) along the short axis of the coal face.

Figure 7 shows that the subsidence trend over time varies at different locations along the mining direction in the coal face. Subsidence activity near the boundary can persist for over 15 years, whereas sampling points closer to the center point, including those on the sampling line perpendicular to the mining direction, tend to level off 5 years after the cessation of coal mining.

Referring to the spatial location relationship of each point shown in Figure 5b, we established the section of cumulative long-term subsidence with time at the sampling lines based on the relationship between cumulative long-term subsidence and duration after coal mining cessation (Figure 7), as shown in Figure 8. The variation in cumulative subsidence along the mining direction (S1–S10) of the extraction area showed significant differences among the sampling points. In the short term after the cessation of coal mining, subsidence was more pronounced closer to the central sampling point (S0). However, over a longer period of time, subsidence movements became more apparent near the boundary locations (Figure 8a), and the subsidence curve exhibits an inclined W-shape. Perpendicular to the mining direction (S11–S18), the cumulative subsidence was relatively consistent in the short term after the cessation of coal mining. However, over time, the cumulative subsidence at the center of the mining area became more pronounced (Figure 8b).

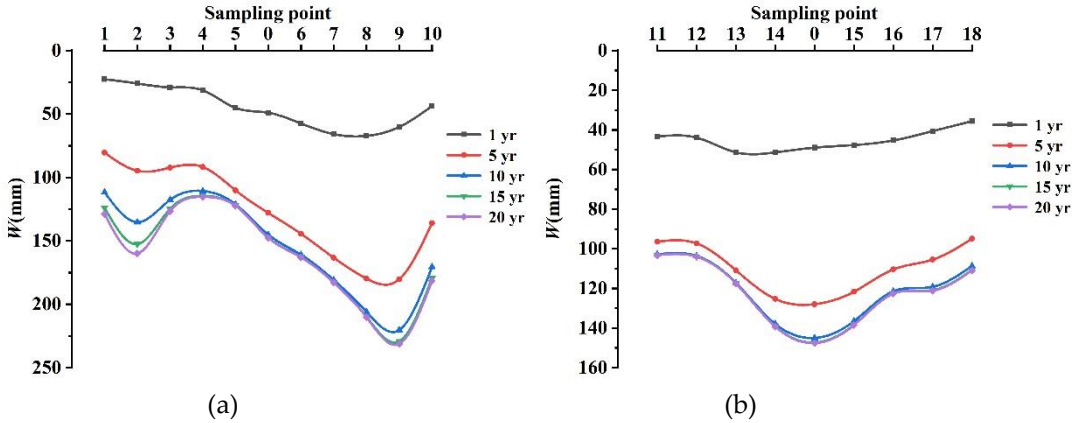

(a) (b)

Figure 8. Cumulative subsidence curve: (a) along the long axis of the coal face; (b) along the short axis of the coal face.

4. Discussion

4.1 Reliability of the proposed method

To verify the reliability of the proposed method in this paper, a spatially independent coal face numbered 81218 was selected. This coal face was located in the northwestern part of the study area

Preprints (www.preprints.org) | NOT PEER-REVIEWED | Posted: 18 July 2023 doi:10.20944/preprints202307.1115.v1

and ceased mining operations in November 2017 (Figure 5a). As subsidence increases sharply within 4 to 5 years after the cessation of coal mining, we processed 50 Single Look Complex (SLC) images obtained from Sentinel-1 using SBAS-InSAR technology to obtain the land subsidence above coal face 81218 from November 2017 to November 2021. To address the monitoring errors caused by the increased processing timespan of radar images, we segmented the long-term radar images into four groups, each comprising 50 views with a timespan of one year. Additionally, we marked the location of coal face 81218 and the contrast reference point in the subsidence cloud diagram, as shown in Figure 9.

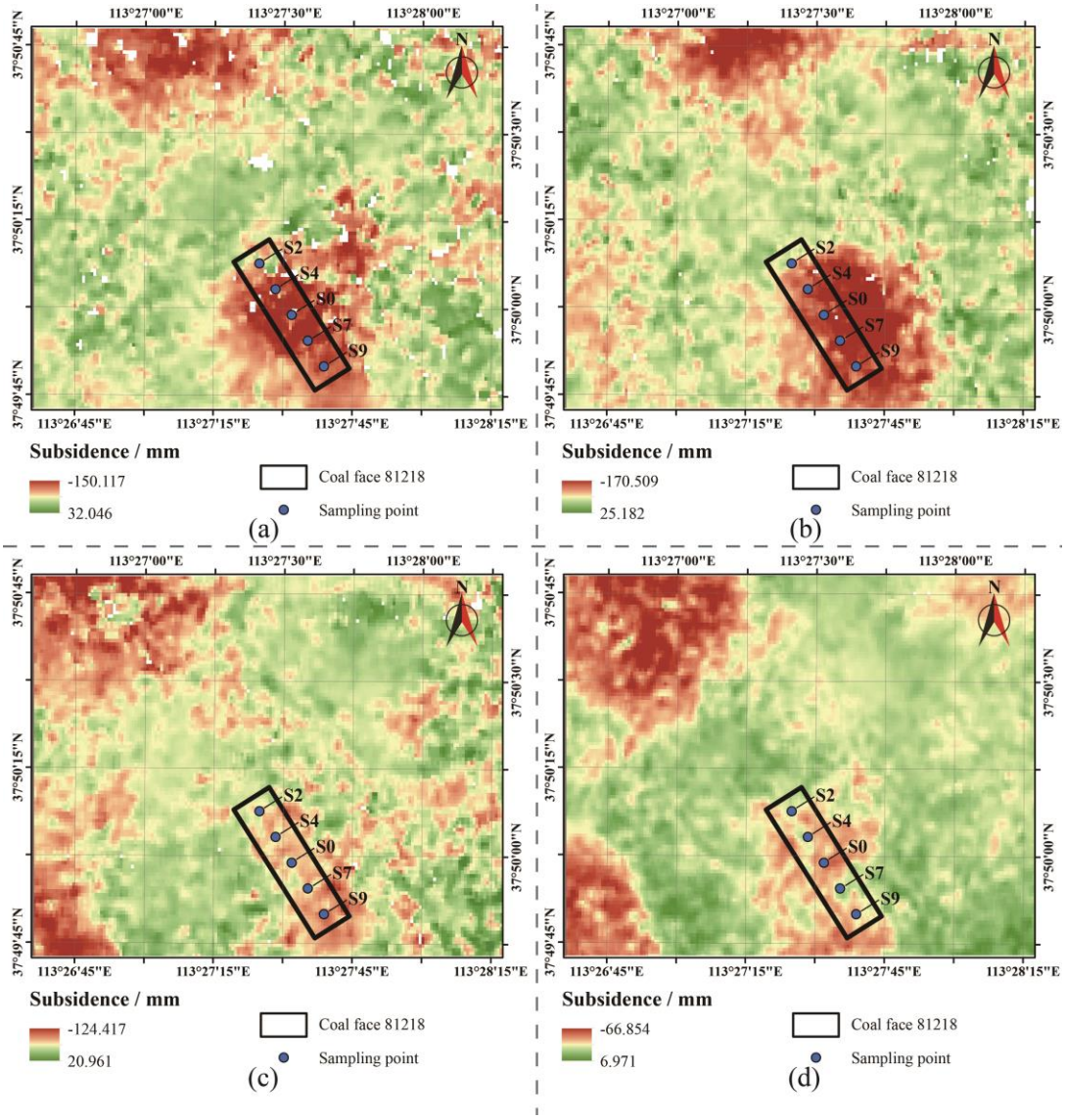

Figure 9. Location of coal face 81218 and subsidence contours (a) from November 2017 to November 2018; (b) from November 2018 to November 2019; (c) from November 2019 to November 2020; and (d) from November 2020 to November 2021.

The layout of sampling lines and points was set consistently across coal face 81218. Considering the different subsidence characteristics of the sampling points shown in Figs. 6, 7, and 8, we selected S2, S4, S0, S7, and S9 along the mining direction to compare the subsidence obtained from the actual monitoring data and predicted the results using the proposed method in this paper. As shown in Figure 10, the actual monitoring data fluctuate slightly along the predicated curve, and the overall change trend is consistent with the predicated curve. In addition, we utilized both correlation analysis and analysis of variance (ANOVA) to evaluate the similarity between the actual monitoring data and the predicted curve. Correlation analysis measures the strength and direction of the relationship

 doi:10.20944/preprints202307.1115.v1

between two variables. The correlation coefficient ranges between −1 and 1, with a result close to 1 indicating a stronger positive correlation, a result close to −1 indicating a stronger negative correlation, and a result close to 0 indicating little to no correlation between the two variables [44]. After conducting a correlation analysis on the two sets of data, we can determine whether the data from both sets show similar change trends. However, correlation analysis alone does not provide information on the significance of any differences between the two datasets. To address this problem, we performed an additional ANOVA step. The ANOVA method is a statistical test that determines whether there are significant differences between the means of two or more groups of data. In the context of comparing two datasets, ANOVA can be used to test for significant differences in their overall values [45]. Table 3 displays the correlation coefficients for each point, all of which are greater than 0.9, indicating a strong correlation between the predicted subsidence results and the monitoring results at each point. Additionally, the ANOVA test performed on each point shows that the F value of the data between sets was much smaller than the critical F value at α=0.05, indicating no significant difference between the values of the two sets at each comparison point. Overall, the proposed method demonstrated reliable and accurate long-term subsidence predictions for the surface of the mined-out collapse area, as evidenced by the close match between the predicted and monitored results.

Preprints (www.preprints.org) | NOT PEER-REVIEWED | Posted: 18 July 2023 doi:10.20944/preprints202307.1115.v1

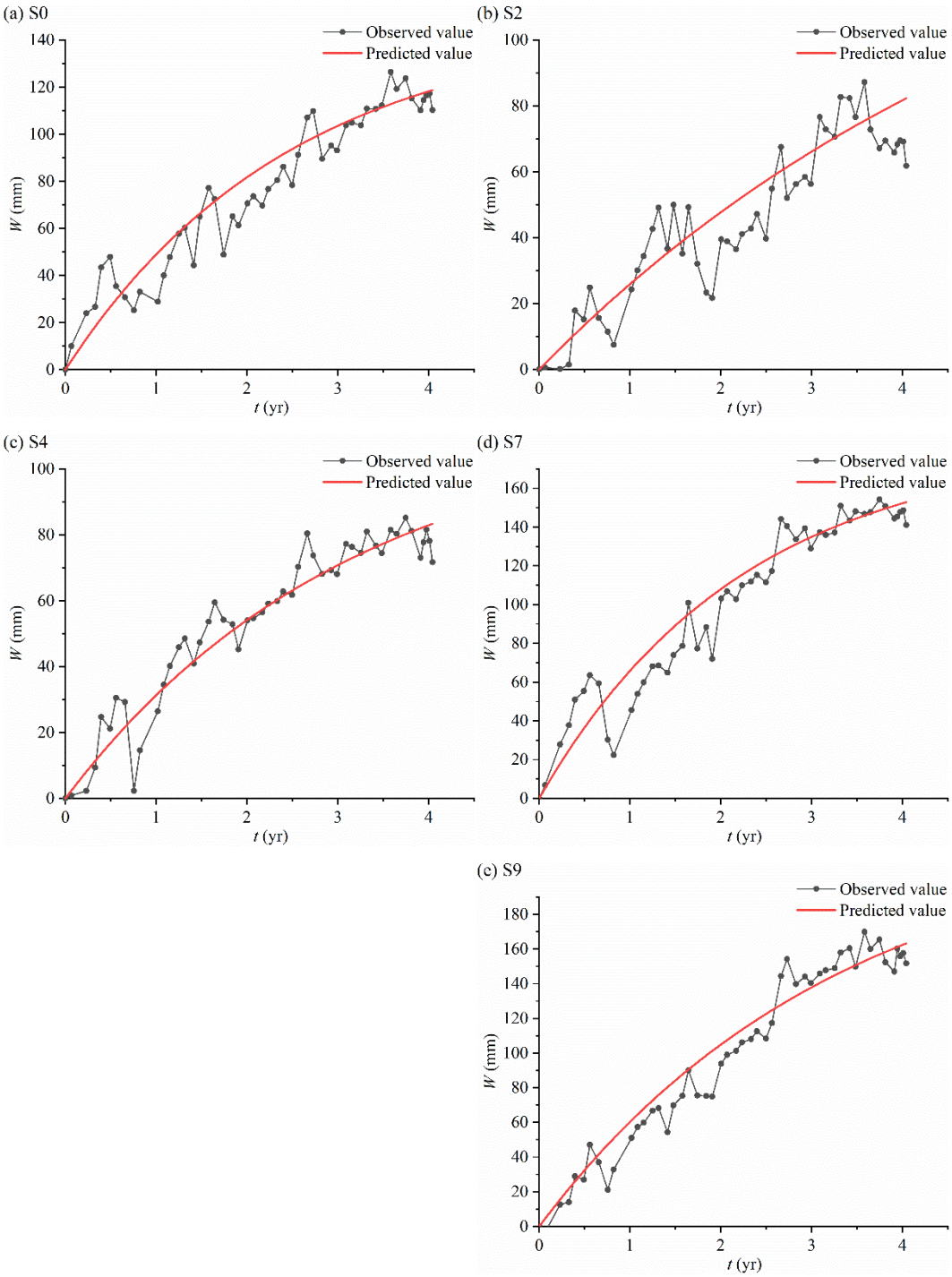

Figure 10. Comparison of predicted results and actual monitoring data.

Table 3. Correlation analysis and ANOVA results of the predicted and monitored datasets.

Point	Correlation Coefficients	ANOVA (α=0.05)	
		F	F_{crit}
S0	0.955135	0.187691	
S2	0.913511	0.721422	
S4	0.963451	0.037546	3.938111
S7	0.95684	0.187504	
S9	0.978571	0.172836	

4.2 Regression parameters of the fitting curve

Preprints (www.preprints.org) | NOT PEER-REVIEWED | Posted: 18 July 2023 doi:10.20944/preprints202307.1115.v1

As indicated by Eq. (1) and Eq. (2), v_0 represents the initial subsidence rate of the sampling points after the cessation of coal mining, which determines the initial subsidence intensity of the sampling points. W_m represents the maximum cumulative subsidence of the sampling points after the cessation of coal mining, which determines the final cumulative subsidence value of the sampling points. c is the time influence factor, which affects the trend of v and W for the sampling points over time. As shown in Figs. 6 and 7, a high value of c leads to a rapid decrease in the velocity (v) of the sampling point during the initial stage following the cessation of coal mining, whereas the parameter W reaches a relatively stable state within a short period of time.

Table 2 shows that the parameters of the sampling points vary with the location of coal face axes. For the sampling points (S1–S10) on the long axis, both v_0 and c show a similar trend of increasing and then decreasing, with maximum value occurring at S7. This regularity can be attributed to two factors: (1) The mining sequence of the coal face. Mining activities follow a certain sequence, and when monitoring land subsidence at the same time, the start time of subsidence differs across different locations. Compared to sampling points with lower numbers (S1–S5), those with higher numbers (S6–S10) experience a shorter timespan and more intense subsidence in the early stages of monitoring. (2) The boundary effect. Due to the influence of the unmined rock layers outside the mining boundary, those near the boundary may produce more cavities that cannot be closed immediately [46], resulting in less significant subsidence at sampling points near the boundary in the initial stages after the cessation of coal mining, compared to those in the middle of the mining area. In contrast, sampling points (S11–S18) along the short axis of the coal face are perpendicular to the mining direction and are not affected by the mining sequence. Due to the short span of the short axis, the distance between each sampling point is relatively short. Therefore, each sampling point is more significantly affected by the boundary, and the changes in the parameters of each sampling point are not significant. Meanwhile, the sampling points close to the center (S0) are less affected by the boundary effect and have a larger v_0 value.

As seen in Figure 8, it is evident that the cumulative subsidence curve along the long axis of the coal face evolves from a subsidence basin into an inclined W-shaped over time. The initial basin shape is consistent with the land subsidence shape after the cessation of coal mining [13]. However, the subsequent inclined W-shape differs from the residual land subsidence prediction results and is the result of the combined effects of the two factors previously mentioned. Traditional prediction methods do not consider the influence of mining sequence [47]. By considering the parameters of the sampling points (Table 2), it is evident that S7 has the largest v_0, whereas S9 has the largest W_m. Meanwhile, S2, which is on the opposite side corresponding to S9, exhibits a local peak in the cumulative subsidence curve. Despite the fact that S7 experienced a significant cumulative subsidence in the initial stages after mining cessation, its subsidence trend slowed down considerably over time. In contrast, S2 and S9 did not undergo significant subsidence during the early stages after mining cessation, but their subsidence rate decreased slowly, resulting in a more substantial final cumulative subsidence (W_m). In terms of the relative horizontal position of the sampling points to the coal face, S7 is close to the center of the coal face, whereas S2 and S9 are close to the edge. Upon ceasing mining, the overlying strata in the center of the coal face underwent more substantial compaction, whereas inadequate compaction can still be observed near the boundary of the coal face. Consequently, the sampling points near the boundary (S2 and S9) exhibited a higher subsidence potential [48]. Moreover, S7 and S9 are in close proximity to each other and have higher serial numbers. Due to the mining sequence of the coal face, the higher-numbered sampling points on the long axis experienced a shorter subsidence time before monitoring, resulting in more pronounced subsidence compared to the smaller-numbered sampling points.

Based on the above analysis, it can be inferred that the cumulative subsidence of the surface near the boundary of the coal face is more significant during long-term subsidence after mining cessation. Therefore, it is recommended to pay more attention to the treatment of the overlying strata and surface above the boundary of the coal face after mining in practical engineering to minimize the post-subsidence impact on the project.

 doi:10.20944/preprints202307.1115.v1

4.3 Applicability of the proposed method

The proposed method for predicting long-term land subsidence in subsidence areas is based on the normalizing, merging, and fitting of short-term InSAR monitoring data obtained from multiple coal faces with different durations after coal mining cessation. This method demonstrates certain advantages in predicting long-term land subsidence in goafs. First, it addresses the difficulty in acquiring continuous and long-term data on surface movement and subsidence in goafs, as monitoring activities in field observation stations often end after the cessation of coal mining to save costs. Second, it avoids increasing the errors incurred when using SBAS-InSAR technology to process long-time-series images, which may lead to significant errors due to the limitations of radar image data, such as atmospheric conditions, vegetation cover, terrain slope, orbit errors, and subsidence gradients. Although the SBAS-InSAR technology is more effective in mitigating the impact of temporal and spatial mismatches on the results, it can also capture surface displacements caused by human activities as monitoring time increases, which may be confused with land subsidence induced by mining. In contrast, the proposed method of using short-term monitoring results to fit land subsidence can effectively avoid these adverse factors, thus improving the accuracy of the prediction results.

Based on the above discussion, we recognize that the proposed method for predicting long-term land subsidence in goafs is advantageous and competitive in some aspects. This prediction method has potential application prospects in situations where there are missing or short monitoring data within a wide range. Meanwhile, this method can effectively eliminate the interference of land subsidence caused by human activities when coal mines stop operation for some time. However, it should be noted that the geological and topographic conditions of different mining areas vary, and the parameters of the prediction model may change due to differences in geological, topographic, and mining conditions. Furthermore, as the values of subsidence parameters are influenced by various factors, future research could explore additional potential influencing factors and refine the prediction models.

5. Conclusions

In this paper, we proposed a method for predicting long-term land subsidence in goafs based on short-term InSAR monitoring data. Using the Yangquan No.2 mine in Shanxi Province, China, as a case study, we provided a detailed description of the application process and investigated the long-term subsidence patterns of the mined-out area. The main conclusions are presented as follows:

(1) The relationship between subsidence rate and duration after coal mining cessation of a coal face conformed to an exponential function, whereas that between the cumulative subsidence and duration after coal mining cessation of a coal face conformed to the Knothe time function;

(2) After the cessation of coal mining, significant land subsidence of the mining area persisted for 5 to 10 years, followed by a trend of stabilization, where the subsidence rate decreased over time. Within the first 5 years, a notable land subsidence was observed in areas situated nearer to the center of the coal face. Subsequently, this area moved towards the boundary of the coal face;

(3) The cumulative subsidence curve along the long axis of the coal face ultimately displays an inclined W-shape, with the peak occurring near the boundary, which might be attributed to the boundary effect. The curve is not symmetrical, with the section closer to the cessation line exhibiting greater subsidence, which might be attributed to the mining sequence of the coal face;

(4) After mining cessation, sustained and significant subsidence motion occurred above the boundary of the coal face, with a large cumulative subsidence. Particular attention should be paid to subsidence motion in this area.

Author Contributions: Conceptualization, N.X.; methodology, M.Z. and G.M.; validation, J.L.; formal analysis, J.L. and S.Y.; investigation, J.L.; resources, G.M.; data curation, J.L.; writing—original draft preparation, J.L. and M.Z.; writing—review and editing, M.Z.; visualization, J.L.; supervision, M.Z. and N.X.; project administration, N.X.; funding acquisition, N.X. All authors have read and agreed to the published version of the manuscript.

Funding: This work was funded by Xiongan New Area Science and Technology Innovation Special Project (2022XAGG0400) and National Natural Science Foundation of China (Grant Nos. 42207215 and 42230709).

Data Availability Statement: Data will be made available on request.

Acknowledgments: The authors thank the Xiongan New Area Science and Technology Innovation Special Project (2022XAGG0400) and the National Natural Science Foundation of China (Grant Nos. 42207215 and 42230709).

Conflicts of Interest: The authors declare that they have no known competing financial interests or personal relationships that could have appeared to influence the work reported in this paper.

References

1. Singh, K. B.; Dhar, B. B. Sinkhole Subsidence Due to Mining. *Geotech. Geol. Eng.* **1997**, *15* (4), 327–341. https://doi.org/10.1007/BF00880712.
2. Bankher, K. A.; Al-Harthi, A. A. Earth Fissuring and Land Subsidence in Western Saudi Arabia. *Nat. Hazards* **1999**, *20* (1), 21–42. https://doi.org/10.1023/A:1008167913575.
3. Du, S.; Wang, Y.; Zheng, M.; Zhou, D.; Xia, Y. Goaf Locating Based on InSAR and Probability Integration Method. *Remote Sens.* **2019**, *11* (7), 812. https://doi.org/10.3390/rs11070812.
4. Chen, B.; Yu, H.; Zhang, X.; Li, Z.; Kang, J.; Yu, Y.; Yang, J.; Qin, L. Time-Varying Surface Deformation Retrieval and Prediction in Closed Mines through Integration of SBAS InSAR Measurements and LSTM Algorithm. *Remote Sens.* **2022**, *14* (3), 788. https://doi.org/10.3390/rs14030788.
5. Guo, Q.; Meng, X.; Li, Y.; Lv, X.; Liu, C. A Prediction Model for the Surface Residual Subsidence in an Abandoned Goaf for Sustainable Development of Resource-Exhausted Cities. *J. Clean. Prod.* **2021**, *279*, 123803. https://doi.org/10.1016/j.jclepro.2020.123803.
6. Yao, X.; Reddish, D. Analysis of Residual Subsidence Movements in the Uk Coalfields. *Q. J. Eng. Geol.* **1994**, *27*, 15–23. https://doi.org/10.1144/GSL.QJEGH.1994.027.P1.04.
7. Sheorey, P. R.; Loui, J. P.; Singh, K. B.; Singh, S. K. Ground Subsidence Observations and a Modified Influence Function Method for Complete Subsidence Prediction. *Int. J. Rock Mech. Min. Sci.* **2000**, *37* (5), 801–818. https://doi.org/10.1016/S1365-1609(00)00023-X.
8. Unlu, T.; Akcin, H.; Yilmaz, O. An Integrated Approach for the Prediction of Subsidence for Coal Mining Basins. *Eng. Geol.* **2013**, *166*, 186–203. https://doi.org/10.1016/j.enggeo.2013.07.014.
9. Mahmoudpour, M.; Khamehchiyan, M.; Nikudel, M. R.; Ghassemi, M. R. Numerical Simulation and Prediction of Regional Land Subsidence Caused by Groundwater Exploitation in the Southwest Plain of Tehran, Iran. *Eng. Geol.* **2016**, *201*, 6–28. https://doi.org/10.1016/j.enggeo.2015.12.004.
10. Álvarez-Fernández, M. I.; González-Nicieza, C.; Menéndez-Díaz, A.; Álvarez-Vigil, A. E. Generalization of the n–k Influence Function to Predict Mining Subsidence. *Eng. Geol.* **2005**, *80* (1–2), 1–36. https://doi.org/10.1016/j.enggeo.2005.02.004.
11. Zhang, L.; Cheng, H.; Yao, Z.; Wang, X. Application of the Improved Knothe Time Function Model in the Prediction of Ground Mining Subsidence: A Case Study from Heze City, Shandong Province, China. *Appl. Sci.-Basel* **2020**, *10* (9), 3147. https://doi.org/10.3390/app10093147.
12. Ghabraie, B.; Ghabraie, K.; Ren, G.; Smith, J. V. Numerical Modelling of Multistage Caving Processes: Insights from Multi-Seam Longwall Mining-Induced Subsidence. *Int. J. Numer. Anal. Methods Geomech.* **2017**, *41* (7), 959–975. https://doi.org/10.1002/nag.2659.
13. Ghabraie, B.; Ren, G.; Zhang, X.; Smith, J. Physical Modelling of Subsidence from Sequential Extraction of Partially Overlapping Longwall Panels and Study of Substrata Movement Characteristics. *Int. J. Coal Geol.* **2015**, *140*, 71–83. https://doi.org/10.1016/j.coal.2015.01.004.
14. Suchowerska Iwanec, A. M.; Carter, J. P.; Hambleton, J. P. Geomechanics of Subsidence above Single and Multi-Seam Coal Mining. *J. Rock Mech. Geotech. Eng.* **2016**, *8* (3), 304–313. https://doi.org/10.1016/j.jrmge.2015.11.007.
15. Ishwar, S. G.; Kumar, D. Application of DInSAR in Mine Surface Subsidence Monitoring and Prediction. *Curr. Sci.* **2017**, *112* (1), 46–51. https://doi.org/10.18520/cs/v112/i01/46-51.
16. Hu, B.; Chen, L.; Zou, Y.; Wu, X.; Washaya, P. Methods for Monitoring Fast and Large Gradient Subsidence in Coal Mining Areas Using SAR Images: A Review. *IEEE Access* **2021**, *9*, 159018–159035. https://doi.org/10.1109/ACCESS.2021.3126787.
17. Zhang, W.; Shi, J.; Yi, H.; Zhu, Y.; Xu, B. Underground Goaf Parameters Estimation by Cross-Iteration with InSAR Measurements. *Remote Sens.* **2021**, *13* (16), 3204. https://doi.org/10.3390/rs13163204.
18. Li, T.; Zhang, H.; Fan, H.; Zheng, C.; Liu, J. Position Inversion of Goafs in Deep Coal Seams Based on DS-InSAR Data and the Probability Integral Methods. *Remote Sens.* **2021**, *13* (15), 2898. https://doi.org/10.3390/rs13152898.

19. Zhao, B.; Guo, Y.; Mao, X.; Zhai, D.; Zhu, D.; Huo, Y.; Sun, Z.; Wang, J. Prediction Method for Surface Subsidence of Coal Seam Mining in Loess Donga Based on the Probability Integration Model. *Energies* **2022**, *15* (6), 2282. https://doi.org/10.3390/en15062282.
20. Can, E.; Kuşcu, Ş.; Mekik, C. Determination of Underground Mining Induced Displacements Using GPS Observations in Zonguldak-Kozlu Hard Coal Basin. *Int. J. Coal Geol.* **2012**, *89*, 62–69. https://doi.org/10.1016/j.coal.2011.08.006.
21. Koros, W. K.; Agustin, F. Subsidence Surveys at Olkaria Geothermal Field, Kenya. *J. Spat. Sci.* **2017**, *62* (1), 195–205. https://doi.org/10.1080/14498596.2016.1191386.
22. Chen, F.; Lin, H.; Zhang, Y.; Lu, Z. Ground Subsidence Geo-Hazards Induced by Rapid Urbanization: Implications from InSAR Observation and Geological Analysis. *Nat. Hazards Earth Syst. Sci.* **2012**, *12* (4), 935–942. https://doi.org/10.5194/nhess-12-935-2012.
23. Dong, J.; Li, H.; Wang, Y.; Zhang, Y. Characteristics and Monitoring-Based Analysis on Deformation Mechanism of Jianshanying Landslide, Guizhou Province, Southwestern China. *Arab. J. Geosci.* **2021**, *14* (3). https://doi.org/10.1007/s12517-021-06473-0.
24. Xu, G.; Gao, Y.; Li, J.; Xing, M. InSAR Phase Denoising: A Review of Current Technologies and Future Directions. *IEEE Geosci. Remote Sens. Mag.* **2020**, *8* (2), 64–82. https://doi.org/10.1109/MGRS.2019.2955120.
25. Xue, F.; Lv, X.; Dou, F.; Yun, Y. A Review of Time-Series Interferometric SAR Techniques: A Tutorial for Surface Deformation Analysis. *IEEE Geosci. Remote Sens. Mag.* **2020**, *8* (1), 22–42. https://doi.org/10.1109/MGRS.2019.2956165.
26. Gabriel, A.; Goldstein, R.; Zebker, H. Mapping Small Elevation Changes Over Large Areas - Differential Radar Interferometry. *J. Geophys. Res.-Solid Earth Planets* **1989**, *94* (B7), 9183–9191. https://doi.org/10.1029/JB094iB07p09183.
27. Wright, P.; Stow, R. Detecting Mining Subsidence from Space. *Int. J. Remote Sens.* **1999**, *20* (6), 1183–1188. https://doi.org/10.1080/014311699212939.
28. Carnec, C.; Delacourt, C. Three Years of Mining Subsidence Monitored by SAR Interferometry, near Gardanne, France. *J. Appl. Geophys.* **2000**, *43* (1), 43–54. https://doi.org/10.1016/S0926-9851(99)00032-4.
29. Yerro, A.; Corominas, J.; Monells, D.; Mallorquí, J. J. Analysis of the Evolution of Ground Movements in a Low Densely Urban Area by Means of DInSAR Technique. *Eng. Geol.* **2014**, *170*, 52–65. https://doi.org/10.1016/j.enggeo.2013.12.002.
30. Berardino, P.; Fornaro, G.; Lanari, R.; Sansosti, E. A New Algorithm for Surface Deformation Monitoring Based on Small Baseline Differential SAR Interferograms. *Ieee Trans. Geosci. Remote Sens.* **2002**, *40* (11), 2375–2383. https://doi.org/10.1109/TGRS.2002.803792.
31. Ferretti, A.; Prati, C.; Rocca, F. Nonlinear Subsidence Rate Estimation Using Permanent Scatterers in Differential SAR Interferometry. *Ieee Trans. Geosci. Remote Sens.* **2000**, *38* (5), 2202–2212. https://doi.org/10.1109/36.868878.
32. Piccialli, F.; Jung, J. E. Understanding Customer Experience Diffusion on Social Networking Services by Big Data Analytics. *Mob. Netw. Appl.* **2017**, *22* (4), 605–612. https://doi.org/10.1007/s11036-016-0803-8.
33. Solaro, G.; Acocella, V.; Pepe, S.; Ruch, J.; Neri, M.; Sansosti, E. Anatomy of an Unstable Volcano from InSAR: Multiple Processes Affecting Flank Instability at Mt. Etna, 1994-2008. *J. Geophys. Res.-Solid Earth* **2010**, *115*, B10405. https://doi.org/10.1029/2009JB000820.
34. Liu, Z.; Mei, G.; Sun, Y.; Xu, N. Investigating Mining-Induced Surface Subsidence and Potential Damages Based on SBAS-InSAR Monitoring and GIS Techniques: A Case Study. *Environ. Earth Sci.* **2021**, *80* (24), 817. https://doi.org/10.1007/s12665-021-09726-z.
35. Fan, H. D.; Cheng, D.; Deng, K. Z.; Chen, B. Q.; Zhu, C. G. Subsidence Monitoring Using D-InSAR and Probability Integral Prediction Modelling in Deep Mining Areas. *Surv. Rev.* **2015**, *47* (345), 438–445. https://doi.org/10.1179/1752270614Y.0000000153.
36. Yang, Z. F.; Li, Z. W.; Zhu, J. J.; Preusse, A.; Yi, H. W.; Wang, Y. J.; Papst, M. An Extension of the InSAR-Based Probability Integral Method and Its Application for Predicting 3-D Mining-Induced Displacements Under Different Extraction Conditions. *Ieee Trans. Geosci. Remote Sens.* **2017**, *55* (7), 3835–3845. https://doi.org/10.1109/TGRS.2017.2682192.
37. Yang, Z. F.; Li, Z. W.; Zhu, J. J.; Hu, J.; Wang, Y. J.; Chen, G. L. InSAR-Based Model Parameter Estimation of Probability Integral Method and Its Application for Predicting Mining-Induced Horizontal and Vertical Displacements. *Ieee Trans. Geosci. Remote Sens.* **2016**, *54* (8), 4818–4832. https://doi.org/10.1109/TGRS.2016.2551779.
38. Saleh, M.; Becker, M. New Estimation of Nile Delta Subsidence Rates from InSAR and GPS Analysis. *Environ. Earth Sci.* **2018**, *78* (1), 6. https://doi.org/10.1007/s12665-018-8001-6.
39. Yang, Z.; Li, Z.; Zhu, J.; Yi, H.; Peng, G.; Hu, J.; Wu, L.; Preusse, A.; Wang, Y.; Papst, M. Locating and Defining Underground Goaf Caused by Coal Mining from Space-Borne SAR Interferometry. *Isprs J. Photogramm. Remote Sens.* **2018**, *135*, 112–126. https://doi.org/10.1016/j.isprsjprs.2017.11.020.

40. Zhang, C.; Zhao, Y.; He, X.; Guo, J.; Yan, Y. Space-Sky-Surface Integrated Monitoring System for Overburden Migration Regularity in Shallow-Buried High-Intensity Mining. *Bull. Eng. Geol. Environ.* **2021**, *80* (2), 1403–1417. https://doi.org/10.1007/s10064-020-02026-z.
41. Murdaca, G.; Rucci, A.; Prati, C. Deep Learning for InSAR Phase Filtering: An Optimized Framework for Phase Unwrapping. *Remote Sens.* **2022**, *14* (19), 4956. https://doi.org/10.3390/rs14194956.
42. Song, S.; Zhao, X.; Xie, J.; Guan, Y. Grey Correlation Analysis and Regression Estimation of Mining Subsidence in Yu-Shen-Fu Mining Area. In *2011 3rd International Conference on Environmental Science and Information Application Technology Esiat 2011, Vol 10, Pt B*; Wu, Y., Ed.; Elsevier Science Bv: Amsterdam, 2011; Vol. 10, pp 1747–1752. https://doi.org/10.1016/j.proenv.2011.09.274.
43. Wang, J.; Zhang, J.; Zhang, Q.; Wu, Z.; Zhang, Q.; Wang, Y.; Gao, D. Analysis of the Control Effect and Parameter Optimisation of Urban Surface Deformation in Underground Coal Mining with Solid Backfilling. *Adv. Civ. Eng.* **2021**, *2021*, 6705685. https://doi.org/10.1155/2021/6705685.
44. Schober, P.; Boer, C.; Schwarte, L. A. Correlation Coefficients: Appropriate Use and Interpretation. *Anesth. Analg.* **2018**, *126* (5), 1763–1768. https://doi.org/10.1213/ANE.0000000000002864.
45. Ostertagová, E.; Ostertag, O. Methodology and Application of Oneway ANOVA. *Am. J. Mech. Eng.* **2013**, *1* (7), 256–261. https://doi.org/10.12691/ajme-1-7-21.
46. Qin, Y.; Xu, N.; Zhang, Z.; Zhang, B. Failure Process of Rock Strata Due to Multi-Seam Coal Mining: Insights from Physical Modelling. *Rock Mech. Rock Eng.* **2021**, *54* (5), 2219–2232. https://doi.org/10.1007/s00603-021-02415-0.
47. Wang, L.; Li, N.; Zhang, X.; Wei, T.; Chen, Y.; Zha, J. Full Parameters Inversion Model for Mining Subsidence Prediction Using Simulated Annealing Based on Single Line of Sight D-InSAR. *Environ. Earth Sci.* **2018**, *77* (5), 161. https://doi.org/10.1007/s12665-018-7355-0.
48. Li, J.; Zang, M.; Xu, N.; Qin, Y.; Chen, Y. Influence of Residual Deformation of Goaf to Sangzhang Tunnel with Probability Integral Method. *J. Eng. Geol.* **2021**, *29* (02), 564–574.